RSC Advances

PAPER

View Article Online
View Journal | View Issue

Cite this: *RSC Adv.*, 2022, **12**, 17784

In vivo characterization of electroactive biofilms inside porous electrodes with MR Imaging†

Luca Häuser, [a] Johannes Erben, [b] Guillaume Pillot, [a] Sven Kerzenmacher, *[a] Wolfgang Dreher [c] and Ekkehard Küstermann [c]

Received 21st February 2022
Accepted 30th May 2022

DOI: 10.1039/d2ra01162j

rsc.li/rsc-advances

Identifying the limiting processes of electroactive biofilms is key to improve the performance of bioelectrochemical systems (BES). For modelling and developing BES, spatial information of transport phenomena and biofilm distribution are required and can be determined by Magnetic Resonance Imaging (MRI) *in vivo*, *in situ* and *in operando* even inside opaque porous electrodes. A custom bioelectrochemical cell was designed that allows MRI measurements with a spatial resolution of 50 μm inside a 500 μm thick porous carbon electrode. The MRI data showed that only a fraction of the electrode pore space is colonized by the *Shewanella oneidensis* MR-1 biofilm. The maximum biofilm density was observed inside the porous electrode close to the electrode-medium interface. Inside the biofilm, mass transport by diffusion is lowered down to 45% compared to the bulk growth medium. The presented data and the methods can be used for detailed models of bioelectrochemical systems and for the design of improved electrode structures.

Introduction

In bioelectrochemical systems (BES), oxidation and/or reduction reactions are catalysed by enzymes or microbes using an electrode as an electron sink or source, respectively.[1–4] Applications for BES comprise the synthesis of chemicals, bioremediation, and energy harvesting.[5–11] Most applications rely on electroactive microbes with the ability of extracellular electron transfer (EET) forming electroactive biofilms (EAB) on electrodes.[12,13] High current densities are generally required for a high production rate and thus for future commercialization of BES.[14–16] While a high amount of biocatalyst *i.e.* a high biofilm density X is a prerequisite for high current densities, the transport of nutrients and reaction products is limited by the biofilm itself.[17–19]

The transport of substrate and reaction products *i.e.* fluxes into and out of the biofilm are linked to the current density according to Faraday's law.[14,20] The fluxes are mainly governed by diffusion which is driven by gradients and coupled with the diffusion coefficient D according to Fick's laws. The gradients result in local chemical microenvironments *e.g.* substrate concentration and pH that effect metabolic activity and therefore current production.[21–23] However, the chemical microenvironment in biofilms has only been measured directly in biofilms grown on flat electrodes mostly using microelectrodes.[24–26] The inside of most porous electrodes cannot be characterized because the material is too fragile (for the use of microelectrodes) or opaque (for characterization with optical tomographic methods, see below). Compared to porous electrodes[8,10] which enable more space for the biofilm and enhanced mass transport, flat electrodes support relatively low current densities and low productivity, but are accessible for such measurements and simple to model.

Such computational biofilm models that include mass transport allow a deeper understanding of the processes occurring in biofilms.[27–29] Existing models of biofilms grown on flat electrodes either rely on parametrization of the biofilm structure, diffusion coefficients and substrate conversion kinetics[10,20,30–34] or make use of spatial information (abstracted profiles of diffusion coefficients) acquired by tomographic imaging techniques.[13,35]

Modelling of complex biofilm structures and its validation requires in-depth information that can be acquired using various tomographic measuring techniques such as Confocal Laser Scanning Microscopy (CLSM),[36–41] Optical Coherence Tomography (OCT)[42–47] and Magnetic Resonance Imaging (MRI).[48] While optical tomographic techniques allow fast and high resolution imaging, only MRI enables the characterization of optically opaque porous electrode/biofilm structures.[45,49–51]

^{1}H-MRI visualizes predominantly water as it is the most abundant molecule with ^{1}H-nuclei. The contrast in MR images depends on structure specific properties of water molecules such as relaxation (*e.g.* T_1, T_2, T_2^*), concentration and diffusion.

[a]*Center for Environmental Research and Sustainable Technology (UFT), University of Bremen, 28359 Bremen, Germany. E-mail: kerzenmacher@uni-bremen.de*

[b]*Electrochaea GmbH, 82152 Planegg, Germany*

[c]*In-vivo-MR Group, Faculty 02 (Biology/Chemistry), University of Bremen, 28359 Bremen, Germany*

† Electronic supplementary information (ESI) available. See https://doi.org/10.1039/d2ra01162j

While water signals are detected from the intra- or extracellular space, the electrode itself does not contribute to the ^{1}H-signal measured and appears in the data as a region with reduced signal intensity. Besides imaging of biofilm structures, MRI enables the monitoring of chemical species, metabolic processes and transport phenomena non-destructively, *in situ* and *in vivo*.[52–59] Thus, it allows the measurement of a variety of quantities relevant to characterization and modelling of electroactive biofilms on porous electrodes. For instance, the MRI measurands – such as relaxation times T_1, T_2 and apparent diffusion coefficients D_* – are indicators for the biofilm density as they differ significantly from the bulk water due to the different physical environments.[53,60] Because the biofilm density X cannot be quantified directly by MRI, empirical correlations of MRI measurands and X are required.

Recently, an *ex vivo* study showed that the biofilm volume (extracted from colonized carbon beads) specified by T_1 correlates with total nitrogen content of the biofilm and the total produced electrical charge.[61] Previously Renslow *et al.* used apparent diffusion coefficients D_* and an empiric correlation[17] to quantify the local biofilm density X.[35] However, the biofilm quantification was not validated. The depth profiles of D_* and X derived from these MRI data were subsequently used to simulate substrate flux, current production and substrate concentration profiles within a *G. sulfurreducens* biofilm grown on a flat electrode.

So far, no study has been published that exploits the benefits of MRI – the *in vivo* imaging of complex EABs inside porous electrodes that are relevant for applications. The present study demonstrates the feasibility of MRI as an *in vivo*, *in situ*, *in operando* and non-invasive method to characterize electroactive biofilms inside porous electrodes. High performance carbon nanofiber electrodes are used which enable high biofilm and current density with *S. oneidensis*.[62–64] The biofilm density and its distribution are analyzed with qualitative indicators, the transversal relaxation time T_2 and the (effective) apparent diffusion coefficient D_* of water. The acquired data, especially the D_* as transport coefficient may, support the 3D modelling of complex biofilms in porous structures.

Materials and methods

We developed a bioelectrochemical reactor suitable for MRI as shown in Fig. 1a and b. The reactor was placed inside the MRI magnet while the nitrogen-purged medium reservoir including medium pump (Ismatec REGLO Digital MS-4/6, Cole-Parmer GmbH, Wertheim, Germany) as well as the potentiostat (Gamry Interface 1010E, C3 Prozess- und Analysentechnik GmbH, Haar, Germany) were located at 4 m distance from the magnet in an adjacent room. The medium feed tube was placed inside a nitrogen gas purged jacket to minimize oxygen intrusion by diffusion. The potentiostat was connected to the electrodes by grounded coaxial wires with non-magnetizing terminal resistors (SRT Resistor Technology GmbH, Cadolzburg, Germany) and tailor-made titanium connectors. The working electrode was mounted in the electrode holder and exposed to the medium at one side. The working electrode ($10 \times 10 \times 0.5$ mm^3) was a high-performance electrode made of electrospun and carbonized nanofibers with a mean diameter of 108 nm and a porosity of 94% (mesopore volume $V_{meso} = 0.24 \times 10^3$ cm^3, mean macropore diameter $d_{macro} = 0.4$ μm, for more details see at Erben *et al.*[63]). A platinum mesh served as counter electrode. The Ag/AgCl reference electrode was made from a silver wire coated with AgCl-suspension inside a LuerLock connector filled with saturated KCl-solution and capped with a glass frit (Gamry, C3 Prozess- und Analysentechnik GmbH, Haar, Germany). The reactor was designed to minimize magnetic field distortions in the region of interest (ROI) by reducing the conductive materials and optimize the alignment of working electrode to the RF coil.

The reactor, the reservoir and lines were filled with 300 ml medium and sterilized by autoclaving at 121 °C for 20 min. Two variants of the medium were used: a standard medium M and an improved medium M* with high phosphate-buffered saline (PBS) content and additional riboflavin (see Table 1 for details). All chemicals were purchased from commercial suppliers, in particular from Sigma-Aldrich (Taufkirchen, Germany), Carl Roth (Karlsruhe, Germany) and Merck (Darmstadt, Germany). After autoclaving the reference electrode was sterilised with 10% hydrogen peroxide solution and then mounted in the reactor under sterile conditions. Before inoculation with *Shewanella oneidensis* MR-1, the contrast agent Gd-DTPA (Magnevist, Bayer AG, Leverkusen, Germany) was added *via* a sterile filter and septum. Magnevist, which is assumed not to enter the bacteria, reduces the T_1 of the medium and total measurement time considerably. By using a TR of 0.5 s the signal originating from the bacterial cytoplasmic compartment, which is expected to have a longer T_1 relaxation time, will be attenuated. This attenuation favours the characterization of the bacterial microenvironment inside the porous electrode. The working electrode was polarized at a potential of 0 V *vs.* Ag/AgCl for at least 12 h prior to inoculation to minimize non-coulombic contributions to the measured current.

S. oneidensis MR-1 cells were precultivated aerobically in Lysogeny Broth (LB medium) and prepared for the use in the bioelectrochemical reactor according to Kipf *et al.*[65] The sterilized reactor was finally inoculated through a sterile septum to get an initial optical density (OD_{600}) of approximately 0.05.

The entire bioreactor was imaged prior to the inoculation for control purposes (abiotic status) and after the bioproduced current density reached its maximum (biotic status) using the same MR sequences and parameters. MR imaging of water was done at 300 MHz (7 T) on a horizontal small-bore MRI system (Bruker Biospec 70/20 USR, Bruker BioSpin MRI, Ettlingen, Germany) with a gradient system of 12 cm inner diameter (B-GA 12S2). For signal transmission and reception, a custom-made, inductively coupled RF-coil (linearly polarized slotted tube resonator) was used which encloses the entire reactor. After adjusting the field homogeneity and RF-power levels the reactor was imaged with two 3D spin-echo (SE) sequences, one with T_2- and a second with diffusion weighting comprising the same field-of-view (FOV) of 19.20 mm × 19.20 mm × 20.0 mm (z y x direction). The FOV is mapped with a resolution of at least 384 × 32 × 33 voxels. This results in a resolution of 50 μm in the z-

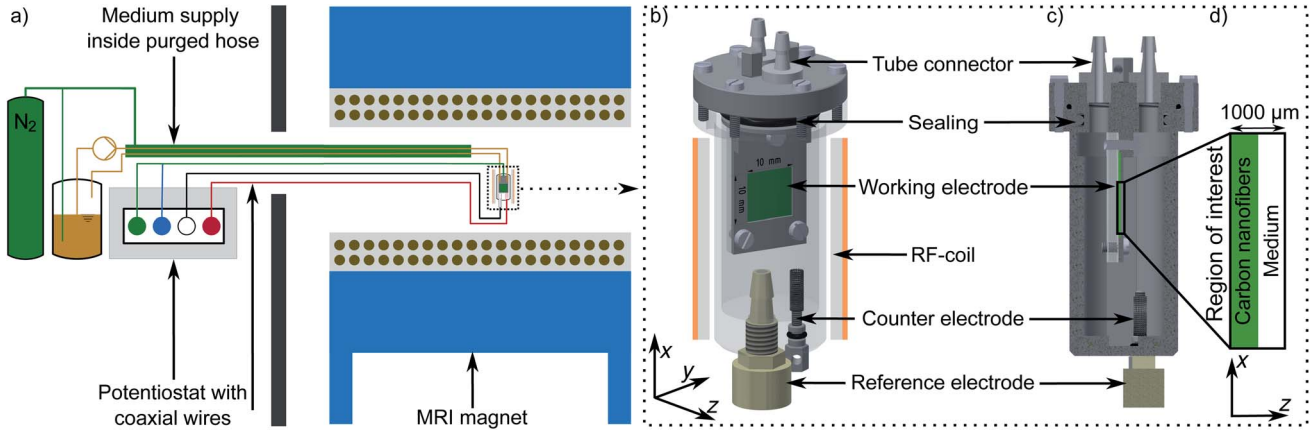

Fig. 1 Schematic drawing of experimental setup: (a) the bioreactor including the potentiostat and the medium reservoir in the room adjacent to the MRI magnet. (b) CAD drawing of the bioreactor in perspective and (c) as cross-section. The bioreactor was located inside the magnet and the RF coil and had a three-electrode design with a working electrode (anode) that was exposed to the medium on one side. The region of interest (d) includes the porous carbon nanofiber electrode and the medium on top of it.

Table 1 Growth media compositions (main differences between the standard medium M and the improved medium M* marked bold)

Component	Concentration c in mmol L^{-1}	
Medium	Standard M	Improved M*
NaCl	137	77
KCl	2.7	2.7
NaHPO	**10**	**40**
$KHPO_4$	**1.76**	**7.04**
$(NH_4)_2SO_4$	9	9
$MgSO_4 \cdot 7H_2O$	1	1
$CaCl_2$	0.1	0.1
Trace elements		
Casein hydrolysate	0.1	0.1
Na-D/L lactate (50% in H_2O)	50	50
Additional components		
Riboflavin	**0**	**0.001**
Contrast agent Magnevist	2	2

direction. Local T_2-values were calculated from SE images obtained with a TR of 0.5 s at 8 echo times TE of 20 ms, 40 ms, 80 ms, 100 ms, 120 ms, 140 ms, 160 ms by fitting the observed signal decay to the equation $S(\mathrm{TE}) = S(0)\exp\{-\mathrm{TE}/T_2\}$. The corresponding 3D-maps of the local self-diffusion constant D_* of water were calculated from 4 images obtained with the so called b-values of 50, 350, 650, and 950 s mm^{-2} fitted to the equation $S(b) = S(0)\exp\{-bD_*\}$, where the b-value describes the diffusion weighting, which can be tuned by strength and duration of the two diffusion sensitizing magnetic field gradients. Prior to data fitting the recorded time domain data was Fourier transformed, masked, filtered, analyzed and graphically represented using custom ImageJ, Matlab and LaTeX scripts. Detailed information on the processing steps is available in the supplementary information (Fig. S1† in ESI).

Relative slice diffusion coefficients $\overline{D_{*,\mathrm{rel}}^{\mathrm{slice}}}$ are (in z-slices/parallel to electrode) averaged slice diffusion coefficients $\overline{D_{*}^{\mathrm{slice}}}$ normalized to their respective value in the medium $\overline{D_{*}^{\mathrm{aq}}}$. $\overline{D_{*,\mathrm{rel}}^{\mathrm{slice}}}$ and relative slice relaxation times $\overline{T_{2,\mathrm{rel}}^{\mathrm{slice}}}$ calculated analogously are unitless and range from 0 to 1.

The depth dependent biofilm density $\overline{X^{\mathrm{slice}}}$ was calculated assuming the relative slice diffusion coefficients $\overline{D_{*,\mathrm{rel}}^{\mathrm{slice}}}$ as diffusion coefficient using the empirical correlation from Fan *et al.*:[17]

$$\overline{D_{*,\mathrm{rel}}^{\mathrm{slice}}} = 1 - \frac{0.43\overline{X^{\mathrm{slice}}}^{0.92}}{11.19 + 0.27\overline{X^{\mathrm{slice}}}^{0.99}} \quad (1)$$

The biofilm density $\overline{X^{\mathrm{slice}}}$ inside the electrode was normalized using the biofilm density $\overline{X_{\mathrm{norm}}^{\mathrm{slice}}}$ of the abiotic uncolonized electrode.

After the MRI experiments the electrode was removed from the reactor, the biofilm was fixated and characterized with fluorescence microscopy and qPCR as control for the biofilm density and its distribution (details in ESI†).[66]

Results and discussion

Two *S. oneidensis* biofilms respiring on and inside porous electrodes in two different media were characterized using T_2-weighted and diffusion-weighted MR imaging to obtain spatial information on biofilm distribution and diffusion coefficients. To demonstrate the MRI capabilities and to visualize biofilm differences, two biofilms were grown using a standard medium M[64,65,67] and an improved medium M* with increased buffer concentration (40 mM PBS) and supplementary riboflavin (1 µM) that stimulates biofilm growth.[67]

The biofilms grown on the electrodes were characterized once the current production had become stable ($t > 120$ h, solid line in Fig. 2a and b). The dotted line represents the current density of the biofilm outside the MRI scanner. Optical density OD_{600} of the media was always below 0.1 (Fig. S8† in ESI) indicating that oxygen input through the reactor and peripherals and the resulting planktonic growth of *S. oneidensis* was negligible.[64]

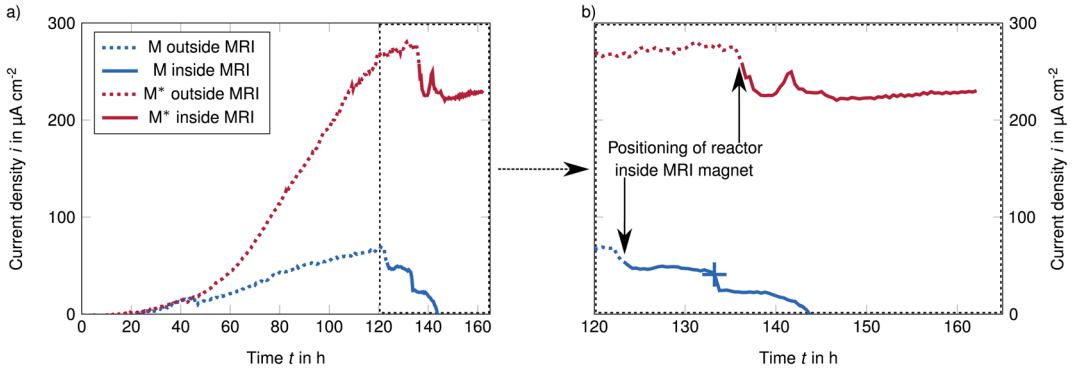

Fig. 2 Chronoamperometry at a potential of 0 mV *vs.* Ag/Cl reveals the rising current as result of *S. oneidensis* use of the electrode as electron acceptor (a) and the feasibility of MRI measurements while operating the bioelectrochemical reactor (b). In the standard medium M an electric defect of the reference electrode (marked with + in (b)) caused the breakdown of the current density, but a control measurement revealed that biofilm was still attached (in ESI†).

Unfortunately, the reference electrode in the experiment with standard medium M was defective, leading to breakdown of the current production (marked with + in Fig. 2b). However, the subsequent control MR imaging (Fig. S7† in ESI) did reveal that the biofilm was still attached to the anode. Therefore, we assume that these experimental results are valid. Our focus was on the biofilm in the improved medium M* while the weak biofilm in the standard medium M should only demonstrate the higher resolution.

Current production during MR imaging

The maximum observed current density i_{max} was 68 µA cm^{-2} in the standard medium M and 280 µA cm^{-2} in the improved medium M*. These current densities are slightly lower than values reported for electron spun material in the literature,[62,64] but higher than Renslows *S. oneidensis* biofilm grown on a flat gold electrode (1.83 µA mm^{-2}).[35] Higher current densities (in both media M and M*) reported by Erben *et al.* are most likely caused by the higher temperature of 30 °C compared to our study (~21 °C). The current increase by a factor of 2 can be well explained by lower metabolic rates due to the temperature difference of about 10 °C to the optimal temperature of 30 °C.[68] The drop in current production after the reactor was positioned from the adjacent room into the MRI magnet (black arrows in Fig. 2b) was probably caused by the temperature difference between the two rooms. The observations described above demonstrate that *in operando* MR image acquisition of live electroactive biofilms within porous electrodes is possible.

T_2-weighted imaging of the bioanode

Fig. 3a shows four representative slices of the region of interest (ROI) covering the porous electrode (slice A) to the growth medium (slices C and D). Slice B represent the electrode with biofilm (visualized for the improved medium M*, standard medium M not shown). The transversal relaxation T_2 is presented as heat maps. The slices are parallel to the electrode/biofilm starting at the back of the electrode, reaching the center and the interface of electrode/medium ($z \leq 500$ µm) and the medium ($z \geq 600$ µm). As the electrode is highly porous and filled with medium the boundary between them is unsharp and illustrated in shades of grey. By averaging all T_2 values in each slice and dividing by T_2^{aq} of water/medium, relative relaxation times $\overline{T_{2,rel}^{slice}}$ of each slice were calculated. Fig. 3b shows a comparison of depth profiles of these $\overline{T_{2,rel}^{slice}}$ for the electrode without biofilm (abiotic control) and with the biofilm in both media M and M*.

In the following the regions of the electrode with biofilm in the improved medium M* are discussed:

- Electrode without biofilm (slice A, $z = 200$ µm):

Slice A is placed at the center of the electrode and shows a rather homogenous T_2 distribution. $\overline{T_{2,rel}^{slice}}$ in this region (slice A) was lower than in the medium (slice C and D, $\overline{T_{2,rel}^{slice}} \sim 1$).

- Electrode with (maximum) biofilm (slice B, $z = 400$ µm):

The averaged $\overline{T_{2,rel}^{slice}}$ with biofilm (in both media M* and M) show a minimum close to the electrode growth medium interface. The minima are not present in the abiotic control (slight decrease is not significant) revealing that the biofilm reduces T_2 relaxation time in accordance with other MRI studies of biofilms.[48] The T_2 heat maps in this region (slice B and Fig. S2† in ESI) show an inhomogeneous distribution indicating an uneven biofilm distribution inside the electrode.

- Growth medium (slice C and D, $z \leq 600$ µm):

$\overline{T_{2,rel}^{slice}}$ is defined as 1 in this region (normalization). $\overline{T_{2,rel}^{slice}}$ in this region is not reduced compared to the abiotic control neither by biofilm nor planktonic cells, indicating low cell densities.

Fig. 3b reveals differences in the biofilm formation for biofilms grown in both media. The biofilm in the improved medium M* is denser and thicker than in the standard medium M according to its lower $\overline{T_{2,rel}^{slice}}$ minimum (0.490 ± 0.018 *vs.* 0.687 ± 0.035) and its broader peak (300 µm *vs.* 250 µm). Please note: all given deviations (value after ±) were calculated based on the standard deviation of their corresponding values in the medium and do not reflect inhomogeneities of the biofilm. The width of the $\overline{T_{2,rel}^{slice}}$ peak in the improved medium M* is mainly caused by the inhomogeneity of the biofilm and in particular by its curved shape (affecting the

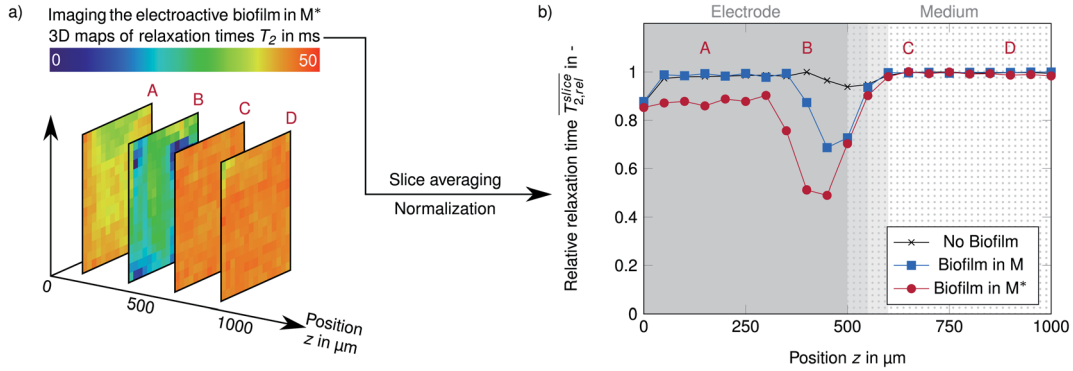

Fig. 3 Relaxation times T_2 of the electrode with and without biofilm revealed by MRI as: (a) 3D heat maps from selected slices parallel to the electrode surface with biofilm (slices A and B) in the improved medium M* (slices C and D) and (b) depth profiles of relative relaxation $\overline{T_{2,rel}^{slice}}$ time against position z for biofilm grown in the standard medium M and in the improved medium M* and without biofilm as abiotic control. $\overline{T_{2,rel}^{slice}}$ was calculated as average of each slice and normalized by the bulk medium relaxation time T_2^{aq}. As the electrode is highly porous (>0.9) and filled with medium the boundary is unsharp and illustrated in shades of grey.

value $T_{2,rel}^{slice}$ minima, see ESI†). The lower $\overline{T_{2,rel}^{slice}}$ minimum in the improved medium M* might be related to the higher concentration of buffer and riboflavin and thus more biofilm mass.[67] In both media, cells were found in the entire electrode (see fluorescence microscopy images Fig. S3† in ESI), but most of the biomass is almost exclusively present close to the interface of electrode to medium.

Accordingly, a large portion of the electrode is not or only marginally colonized by the biofilm. Hence, the total biofilm density and thereby the amount of biocatalyst in the electrode could be higher. The location of the biofilm at the electrode surface might be related to limited diffusive transport of nutrients into the depth of the fiber-biofilm structure and products, especially protons, out of it. To investigate this issue in the next section spatially resolved relative diffusion coefficients $\overline{D_{*,rel}^{slice}}$ were determined and calculated analogously to the determination of relative relaxation times $\overline{T_{2,rel}^{slice}}$.

Diffusion inside the porous electrode without and with biofilm

Fig. 4a shows depth profile of the relative diffusion coefficient $\overline{D_{*,rel}^{slice}}$ (see Materials and methods section) without and with biofilms in the standard medium M and in the improved medium M*. The profiles of the relative diffusion coefficients are similar to the relaxation times (Fig. 3b): For the uncolonized and the colonized electrode, $\overline{D_{*,rel}^{slice}}$ inside the center of the electrode ($z \leq 300$ µm) is similar to $\overline{D_{*,rel}^{slice}}$ in the growth medium ($z \leq 600$ µm) as the pores of the electrode are filled with medium (porosity >90%). A relative diffusion coefficient of 1 corresponds to a water diffusion coefficient D_*^{aq} of 2.00 $10^{-9} \pm$ 0.17 10^{-9} m^2 s^{-1} in the standard medium M and 1.94 $10^{-9} \pm$ 0.09 10^{-9} m^2 s^{-1} in the improved medium M* related to temperatures of approximately 22 °C and 21 °C.[69]

The diffusion near the boundary between electrode and medium is reduced as compared to the electrode center and the growth medium. The minimum of the relative diffusion coefficient $\overline{D_{*,rel}^{slice}}$ in the improved medium M* is lower as compared to the standard medium M ($0.448 \pm 0.056 < 0.713 \pm 0.087$). The minima of the diffusion coefficients are in the same distance from the electrode surface as the minima of the relaxation times $\overline{T_{2,rel}^{slice}}$. T_2 and D_* heat maps as well as the $\overline{T_{2,rel}^{slice}}$ and $\overline{D_{*,rel}^{slice}}$ profiles show a very high similarity. This similarity is in part caused by the diffusion weighting bias brought by the strong magnetic field gradients required for high resolution imaging.[70] This effect attenuates T_2-values of areas with unhindered diffusion more than those of diffusion restricted areas. Nevertheless, the well-known link of biofilm density and restricted diffusion[17,19] is confirmed by the correlation of $\overline{T_{2,rel}^{slice}}$ and $\overline{D_{*,rel}^{slice}}$ (Fig. S6† in ESI).

The morphology and diffusion coefficients of the EABs grown inside porous electrodes in our study differ from the *S. oneidensis* biofilm grown on a flat surface analyzed with MRI by Renslow *et al.*[35] Since biofilm formation from *S. oneidensis* on gold electrodes is often difficult, Renslow *et al.* pre-cultured a biofilm with a constant depth film fermenter, harvested it and transplanted it into the MRI reactor. For this reason, their biofilm exhibited a heterogenous morphology with individual biofilm clusters that settled on the flat gold electrode. In our case it has to be considered, that the colonization of individual *S. oneidensis* cells is different to the attachment of cell clusters, and that the colonization of cells inside electrospun carbon fibers is enhanced compared to a flat electrode. Therefore, the structure and the diffusion coefficients of our biofilms are more comparable to the uniform shape of Renslow's *Geobacter sulfurreducens* biofilm: it has a dense core, but in contrast to the *G. sulfurreducens* biofilm, the diffusion coefficients inside the *S. oneidensis* biofilm decrease on both, the fluid facing and the opposite sides. This underlines: biofilm properties such as morphology and diffusion coefficients vary substantially depending on the electrode and the cultivation conditions. While on a flat surface the EAB only has a limited surface for extracellular electron transfer (EET), an EAB inside a porous electrode can use more electrode volume for EET and that could support uniform biofilm growth within the electrode and more current production.

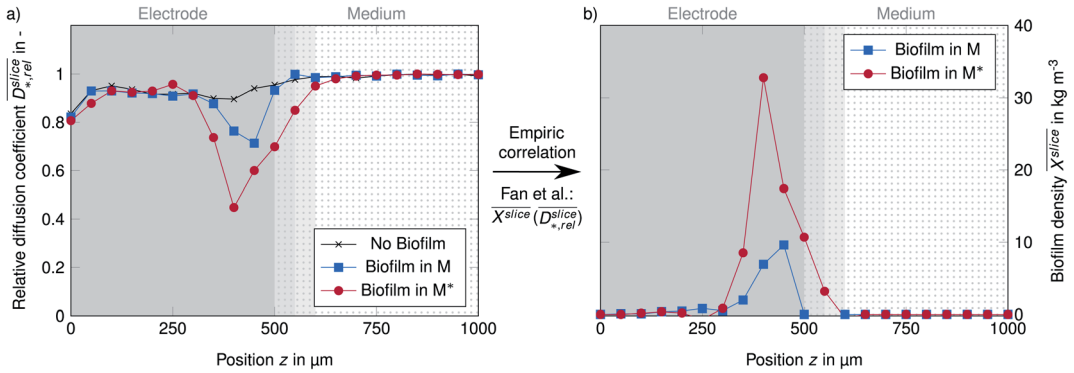

Fig. 4 Relative diffusion coefficients $\overline{D^{slice}_{*,rel}}$ calculated from diffusion weighted MRI plotted against position z (a). $\overline{D^{slice}_{*,rel}}$ and the empiric correlation from Fan *et al.* are used to calculate spatial biofilm density $\overline{X^{slice}}$ distribution (b).

In porous materials with a high biofilm density and thus a high current production, proton transport from the individual cells to the bulk can become rate-limiting. Under such conditions, not only the electrode has an influence on the biofilm formation, but also the medium:[67] assuming the same biofilm density, higher buffer capacity in the improved medium M* enhances diffusive transport of protons or the corresponding buffer molecules and thus provides lower local acidification of the anodic biofilm in the improved medium M* as compared to the standard medium M (lower buffer concentration). This allows the biofilm in the improved medium M* to continue to grow and to increase its density until its local acidification reaches the level of the biofilm in the standard medium M. Thus, high puffer capacities allow high diffusive proton transport rates and thus more biofilm mass.[67]

The higher biofilm mass could lead to a homogeneous distribution in the electrode (thicker biofilm) or to an increase in biofilm density in the front region (denser biofilm). The local increase of the biofilm density in the front region is equivalent to an increase in the biocatalyst in the region. Thus, the volumetric production of electrons and protons also increases. In this case, the protons are more concentrated in the front region. According to Fick's 1st law of diffusion, a steeper gradient in denser biofilms results in higher transport fluxes and thus higher currents.

We observed exactly that: the biofilm is mainly located around the interface of electrode and growth medium (see also fluorescence microscopy images in Fig. S3† in ESI) and higher buffer capacity result in a denser, but not thicker biofilms. This is well in line with Erben *et al.*[64] who investigated the biofilm formation on the same material: under anaerobic conditions (OD < 0.1, similar to our experiments) more biofilm was found at the front (medium facing) side than on the backside as observed by scanning electron microscopy (SEM).[64] However, the imaging techniques like SEM or fluorescence microscopy used in this context only provide information about the first few micrometers in depth. In contrast to these methods, MR imaging covers the entire volume and has previously been used to quantify the biofilm density.[35,58] Unlike other bulk-based methods using dry weight, total nitrogen content, qPCR or protein analysis,[13,46,50,61] the determination of biofilm density based on correlation of MRI parameters is *in situ* and non-destructive.

Biofilm density distribution inside the porous electrode

Assuming the validity of the frequently used empirical correlation of Fan *et al.* (see eqn (1), Materials and methods section) the biofilm density $\overline{X^{slice}}$ was calculated with $\overline{D^{slice}_{*,rel}}$. In Fig. 4b for both media, the profile of the biofilm density $\overline{X^{slice}}$ is plotted against the z-axis. The empirical relation translates low $\overline{D^{slice}_{*,rel}}$ to high biofilm densities. Thus, the maximum biofilm density coincides with $\overline{D^{slice}_{*,rel}}$ minima inside the electrode. Due to the lower $\overline{D^{slice}_{*,rel}}$ values, in the improved medium M* the maximum biofilm density $\overline{X^{slice}}$ = 32.8 (28.8, 40.7) kg m^{-3} is higher than 9.6 (7.1, 17.1) kg m^{-3} determined in the standard medium M with lower buffer concentration. The values in brackets reflect the deviation of the biofilm density calculations and are based on the standard deviations of the relative diffusion coefficients in the medium. The upper limit is higher because the empirical Fan correlation is not linear.

The results of the Fan's empirical relationship and in particular the quantitative results should be treated with caution for at least three reasons:

- First, this relationship was derived from the characterization of aerobic biofilms on smooth surfaces, rotating cylinders, and bioflocs.[17] The conditions in our experiments differ significantly: the use of porous 3D electrodes and a facultative anaerobic organism with a metabolism based on external electron transfer might result in different cell densities, Extracellular Polymeric Substance (EPS) and the production of conductive appendages, affecting the density of the biomass.
- Second, the diffusion coefficients for the entire biofilm were specified mostly using diffusion reaction models and diffusion cells, which both measure the transport of a specific species trough a compartment.[17] This might differ significantly from the MRI approach determining the self-movement of water molecules in a compartment/sub volume/voxel.
- Third, compared to bulk diffusion coefficients the spatially resolved diffusion coefficients might be biased due to the non-linearity of the empiric correlation (Fig. S4f and S5† in ESI).

Thus, variances introduced by higher noise levels at high resolution, subvolumes and the biofilm inhomogeneity can lead to different biofilm densities (discussed in ESI†).

• Fourth, the model from Fan *et al.* has been derived from data measuring the diffusion in the extracellular space of the biofilm. Similarly, in the present study the signal from the bacterial cytoplasm is attenuated due to the addition of the contrast agent Gd-DTPA, which reduces only the T_1-relaxation time of the medium. Thus, the estimated diffusion coefficients are biased to the extracellular space which justifies to use the Fan model in order to calculate the biofilm density.

Therefore, it is even more important to validate the biofilm densities and their distribution determined by diffusion weighted MRI and the Fan correlation. For example, the cell count (not including EPS-matrix) or the total biomass in the electrode can be determined using qPCR assays or determination of the total nitrogen content.[61,71,72] The validation we applied by qPCR and correlation of current per biomass (see ESI† for details) cannot confirm quantitatively the biofilm density but show a similar trend of a higher biofilm density in the improved medium M*.

Limitations of an electroactive biofilm in a porous fiber electrode

The amount of current produced depends on the amount of biocatalyst or biofilm mass.[64] Certain materials with a high attractiveness of the anodic habitat, such as the porous carbon nanofiber electrode used here, stimulate biofilm formation and current production, especially for *S. oneidensis*.[62,64,73,74]

In this study, MRI demonstrated that the ability of the porous electrospun electrode to host biofilm is not fully exploited. The determined biofilm density distribution within electrodes is inhomogeneous, as mostly the region around the interface of electrode to medium is colonized. The porous electrode could thus host higher biofilm densities in the deeper region, but also in the front region the biofilm density could thus be higher as a comparison to other biofilms shows.[35] The question remains why only a part of the electrode is colonized and what can be deduced from the shape of the biofilm.

The transport through the biofilm is restricted by the biofilm itself. The consequence of the restricted diffusive transport in the biofilm and metabolism of the cells is the formation of a concentration gradient. Gradients in the electrode create microenvironments which influence the metabolism, the current production and the biofilm formation.[2,13,23,24,75]

For instance, if fresh medium with dissolved oxygen is present at the liquid facing side, in the anaerobic depth of the biofilm the terminal electron acceptor (TEA) is the electrode where the aerobic toplayer uses dissolved oxygen as TEA.[76] Moreover, the directional motility of cells may prevent penetrating deeper due to the higher redox potential of oxygen compared to the potential of the anode.[77] However, the observed optical density $OD_{600} < 0.1$ in the growth medium does not indicate a high amount of dissolved oxygen (Fig. S7† in ESI).

Biofilm formation in deep layers could also be prevented by the arising pH gradients/local acidification in deep layers of the biofilm/electrode.[67] However, increasing the buffer concentration (from standard medium M to improved medium M*) does not, or only slightly, cause the biofilm to penetrate deeper into the electrode – instead, the biofilm density increases. But even in the improved medium M*, the biofilm density is not high enough to restrict transport of protons in the electrode completely. This can be deduced from the fact that the relative relaxation times $\overline{T_{2,\mathrm{rel}}^{\mathrm{slice}}}$ and diffusion coefficients $\overline{D_{*,\mathrm{rel}}^{\mathrm{slice}}}$ are reduced by a maximum of 55% inside the biofilm. Denser and not thicker biofilms enhance diffusive transport fluxes because the driving forces *i.e.*, concentration gradients are higher. The higher transport flux of protons and their corresponding buffer molecules lead to higher current densities.

Thus, further research is needed to understand the specific connection between concentration gradients and biofilm formation in porous electrodes. Advanced NMR methods such as spectroscopic imaging, chemical exchange saturation transfer (CEST) and electrophoretic NMR in combination with electrochemical methods can further elucidate the dynamics of and inside the biofilm and its performance in bioelectrochemical systems.[2,78–81]

Conclusions

In this study we present a biochemical reactor for the non-destructive, *in vivo* and *in situ* characterization of electroactive biofilms with Magnetic Resonance Imaging. For the first time, we show the feasibility of MRI inside porous electrodes. We demonstrate that the MR image acquisition is possible while the reactor serves as a bioelectrochemical cell. The biofilm reduced both transversal relaxation times T_2 and apparent diffusion coefficients D_*. The spatial biofilm density can be qualitatively estimated from the T_2 or D_* values. Furthermore, a quantitative determination *via* relative T_2 and D_* and empirical correlations is possible but requires further research. In an improved medium M* with a higher buffer concentration the biofilm produced more biomass (lower T_2 and D_*) and higher current density. The MRI method was able to reveal that only a fraction – the upper, fluid facing side – of the electrode was colonized by the biofilm leading to low current densities. In conclusion, this study showed that MRI is a versatile method for the characterization and development of electroactive biofilms inside porous, opaque electrodes.

Conflicts of interest

There are no conflicts to declare.

Acknowledgements

We gratefully acknowledge financial support from the German Research Association DFG through the priority programme SPP 2240: eBiotech (project: 445813859, grant numbers: KE 1576/5-1 and DR 298/15-1). Furthermore, the authors want to thank SRT Resistor Technology GmbH for providing non-magnetizing resistors and Hanseatische Waren Handelsgesellschaft mbH & Co. KG for providing titanium raw materials.

Notes and references

1 B. E. Logan, B. Hamelers, R. Rozendal, U. Schröder, J. Keller, S. Freguia, P. Aelterman, W. Verstraete and K. Rabaey, Microbial fuel cells: methodology and technology, *Environ. Sci. Technol.*, 2006, **40**, 5181–5192.

2 *Bioelectrochemical systems. From extracellular electron transfer to biotechnological application*, K. Rabaey, L. T. Angenent, U. Schröder and J. Keller, ed. IWA Publishing, London, New York, 2010, ISBN: 9781843392330.

3 F. Harnisch and U. Schröder, From MFC to MXC: chemical and biological cathodes and their potential for microbial bioelectrochemical systems, *Chem. Soc. Rev.*, 2010, **39**, 4433–4448.

4 H. V. M. Hamelers, A. ter Heijne, T. H. J. A. Sleutels, A. W. Jeremiasse, D. P. B. T. B. Strik and C. J. N. Buisman, New applications and performance of bioelectrochemical systems, *Appl. Microbiol. Biotechnol.*, 2010, **85**, 1673–1685.

5 V. Shah, *Emerging environmental technologies*, Springer, New York, 2008.

6 H. Wang and Z. J. Ren, A comprehensive review of microbial electrochemical systems as a platform technology, *Biotechnol. Adv.*, 2013, **31**, 1796–1807.

7 A. Schievano, T. Pepé Sciarria, K. Vanbroekhoven, H. de Wever, S. Puig, S. J. Andersen, K. Rabaey and D. Pant, Electro-Fermentation - Merging Electrochemistry with Fermentation in Industrial Applications, *Trends Biotechnol.*, 2016, **34**, 866–878.

8 C. Santoro, C. Arbizzani, B. Erable and I. Ieropoulos, Microbial fuel cells: From fundamentals to applications. A review, *J. Power Sources*, 2017, **356**, 225–244.

9 G. Kumar, R. G. Saratale, A. Kadier, P. Sivagurunathan, G. Zhen, S.-H. Kim and G. D. Saratale, A review on bio-electrochemical systems (BESs) for the syngas and value added biochemicals production, *Chemosphere*, 2017, **177**, 84–92.

10 F. Harnisch and D. Holtmann, *Bioelectrosynthesis*, Springer International Publishing, Cham, 2019.

11 T. J.-P. Ivase, B. B. Nyakuma, O. Oladokun, P. T. Abu and M. N. Hassan, Review of the principal mechanisms, prospects, and challenges of bioelectrochemical systems, *Environ. Prog. Sustainable Energy*, 2020, **39**, 13298.

12 A. P. Borole, G. Reguera, B. Ringeisen, Z.-W. Wang, Y. Feng and B. H. Kim, Electroactive biofilms: Current status and future research needs, *Energy Environ. Sci.*, 2011, **4**, 4813.

13 H. Beyenal and J. T. Babauta, *Biofilms in bioelectrochemical systems. From laboratory practice to data interpretation*, John Wiley & Sons Inc, Hoboken, 2015.

14 P. N. Bartlett, *Bioelectrochemistry. Fundamentals, experimental techniques and applications*, John Wiley & Sons, Chichester England, Hoboken NJ, 2008.

15 T. H. J. A. Sleutels, A. ter Heijne, C. J. N. Buisman and H. V. M. Hamelers, Bioelectrochemical systems: an outlook for practical applications, *ChemSusChem*, 2012, **5**, 1012–1019.

16 M. M. Ghangrekar and P. Chatterjee, A Systematic Review on Bioelectrochemical Systems Research, *Curr. Pollut. Rep.*, 2017, **3**, 281–288.

17 L. S. Fan, R. Leyva-Ramos, K. D. Wisecarver and B. J. Zehner, Diffusion of phenol through a biofilm grown on activated carbon particles in a draft-tube three-phase fluidized-bed bioreactor, *Biotechnol. Bioeng.*, 1990, **35**, 279–286.

18 P. S. Stewart, A review of experimental measurements of effective diffusive permeabilities and effective diffusion coefficients in biofilms, *Biotechnol. Bioeng.*, 1998, **59**, 261–272.

19 H. Horn and E. Morgenroth, Transport of oxygen, sodium chloride, and sodium nitrate in biofilms, *Chem. Eng. Sci.*, 2006, **61**, 1347–1356.

20 C. I. Torres, A. K. Marcus, P. Parameswaran and B. E. Rittmann, Kinetic experiments for evaluating the Nernst-Monod model for anode-respiring bacteria (ARB) in a biofilm anode, *Environ. Sci. Technol.*, 2008, **42**, 6593–6597.

21 C. I. Torres, A. Kato Marcus and B. E. Rittmann, Proton transport inside the biofilm limits electrical current generation by anode-respiring bacteria, *Biotechnol. Bioeng.*, 2008, **100**, 872–881.

22 A. K. Marcus, C. I. Torres and B. E. Rittmann, Analysis of a microbial electrochemical cell using the proton condition in biofilm (PCBIOFILM) model, *Bioresour. Technol.*, 2011, **102**, 253–262.

23 S. C. Popat and C. I. Torres, Critical transport rates that limit the performance of microbial electrochemistry technologies, *Bioresour. Technol.*, 2016, **215**, 265–273.

24 J. T. Babauta, H. D. Nguyen, T. D. Harrington, R. Renslow and H. Beyenal, pH, redox potential and local biofilm potential microenvironments within Geobacter sulfurreducens biofilms and their roles in electron transfer, *Biotechnol. Bioeng.*, 2012, **109**, 2651–2662.

25 J. T. Babauta and H. Beyenal, Local Current Variation by Depth in Geobacter Sulfurreducens Biofilms, *J. Electrochem. Soc.*, 2014, **161**, H3070–H3075.

26 J. Hou, Z. Liu, Y. Zhou, W. Chen, Y. Li and L. Sang, An experimental study of pH distributions within an electricity-producing biofilm by using pH microelectrode, *Electrochim. Acta*, 2017, **251**, 187–194.

27 D. Deb, R. Patel and V. E. Balas, A Review of Control-Oriented Bioelectrochemical Mathematical Models of Microbial Fuel Cells, *Processes*, 2020, **8**, 583.

28 E. M. Gaffney, M. Grattieri, Z. Rhodes and S. D. Minteer, Editors' Choice—Review—Exploration of Computational Approaches for Understanding Microbial Electrochemical Systems: Opportunities and Future Directions, *J. Electrochem. Soc.*, 2020, **167**, 65502.

29 S. Luo, H. Sun, Q. Ping, R. Jin and Z. He, A Review of Modeling Bioelectrochemical Systems: Engineering and Statistical Aspects, *Energies*, 2016, **9**, 111.

30 C. Picioreanu, I. M. Head, K. P. Katuri, M. C. M. van Loosdrecht and K. Scott, A computational model for biofilm-based microbial fuel cells, *Water Res.*, 2007, **41**, 2921–2940.

31 A. Kato Marcus, C. I. Torres and B. E. Rittmann, Conduction-based modeling of the biofilm anode of a microbial fuel cell, *Biotechnol. Bioeng.*, 2007, **98**, 1171–1182.
32 A. K. Marcus, C. I. Torres and B. E. Rittmann, Evaluating the impacts of migration in the biofilm anode using the model PCBIOFILM, *Electrochim. Acta*, 2010, **55**, 6964–6972.
33 B. Korth, L. F. M. Rosa, F. Harnisch and C. Picioreanu, A framework for modeling electroactive microbial biofilms performing direct electron transfer, *Bioelectrochemistry*, 2015, **106**, 194–206.
34 W.-F. Cai, J.-F. Geng, K.-B. Pu, Q. Ma, D.-W. Jing, Y.-H. Wang, Q.-Y. Chen and H. Liu, Investigation of a two-dimensional model on microbial fuel cell with different biofilm porosities and external resistances, *Chem. Eng. J.*, 2018, **333**, 572–582.
35 R. Renslow, J. Babauta, P. Majors and H. Beyenal, Diffusion in biofilms respiring on electrodes, *Energy Environ. Sci.*, 2013, **6**, 595–607.
36 D. de Beer, P. Stoodley, F. Roe and Z. Lewandowski, Effects of biofilm structures on oxygen distribution and mass transport, *Biotechnol. Bioeng.*, 1994, **43**, 1131–1138.
37 H. Beyenal, C. Donovan, Z. Lewandowski and G. Harkin, Three-dimensional biofilm structure quantification, *J. Microbiol. Methods*, 2004, **59**, 395–413.
38 F. Waharte, K. Steenkeste, R. Briandet and M.-P. Fontaine-Aupart, Diffusion measurements inside biofilms by image-based fluorescence recovery after photobleaching (FRAP) analysis with a commercial confocal laser scanning microscope, *Appl. Environ. Microbiol.*, 2010, **76**, 5860–5869.
39 A. Jain, G. Gazzola, A. Panzera, M. Zanoni and E. Marsili, Visible spectroelectrochemical characterization of Geobacter sulfurreducens biofilms on optically transparent indium tin oxide electrode, *Electrochim. Acta*, 2011, **56**, 10776–10785.
40 A. A. Carmona-Martínez, F. Harnisch, U. Kuhlicke, T. R. Neu and U. Schröder, Electron transfer and biofilm formation of Shewanella putrefaciens as function of anode potential, *Bioelectrochemistry*, 2013, **93**, 23–29.
41 J. Hauth, J. Chodorski, A. Wirsen and R. Ulber, Improved FRAP measurements on biofilms, *Biophys. J.*, 2020, **118**, 2354–2365.
42 M. Wagner, B. Manz, F. Volke, T. R. Neu and H. Horn, Online assessment of biofilm development, sloughing and forced detachment in tube reactor by means of magnetic resonance microscopy, *Biotechnol. Bioeng.*, 2010, **107**, 172–181.
43 M. Wagner, D. Taherzadeh, C. Haisch and H. Horn, Investigation of the mesoscale structure and volumetric features of biofilms using optical coherence tomography, *Biotechnol. Bioeng.*, 2010, **107**, 844–853.
44 F. Blauert, H. Horn and M. Wagner, Time-resolved biofilm deformation measurements using optical coherence tomography, *Biotechnol. Bioeng.*, 2015, **112**, 1893–1905.
45 M. Wagner and H. Horn, Optical coherence tomography in biofilm research: A comprehensive review, *Biotechnol. Bioeng.*, 2017, **114**, 1386–1402.
46 S. D. Molenaar, T. Sleutels, J. Pereira, M. Iorio, C. Borsje, J. A. Zamudio, F. Fabregat-Santiago, C. J. N. Buisman and A. ter Heijne, In situ Biofilm Quantification in Bioelectrochemical Systems by using Optical Coherence Tomography, *ChemSusChem*, 2018, **11**, 2171–2178.
47 M. Hackbarth, T. Jung, J. E. Reiner, J. Gescher, H. Horn, A. Hille-Reichel and M. Wagner, Monitoring and quantification of bioelectrochemical Kyrpidia spormannii biofilm development in a novel flow cell setup, *Chem. Eng. J.*, 2020, **390**, 124604.
48 M. P. Herrling, S. Lackner, H. Nirschl, H. Horn and G. Guthausen, in *Annual Reports on NMR Spectroscopy*, ed. G. A. Webb, Academic Press [Imprint]; Elsevier Science & Technology, Oxford, 2019, pp. 163–213.
49 T. R. Neu, B. Manz, F. Volke, J. J. Dynes, A. P. Hitchcock and J. R. Lawrence, Advanced imaging techniques for assessment of structure, composition and function in biofilm systems, *FEMS Microbiol. Ecol.*, 2010, **72**, 1–21.
50 J. Azeredo, N. F. Azevedo, R. Briandet, N. Cerca, T. Coenye, A. R. Costa, M. Desvaux, G. Di Bonaventura, M. Hébraud, Z. Jaglic, M. Kačániová, S. Knøchel, A. Lourenço, F. Mergulhão, R. L. Meyer, G. Nychas, M. Simões, O. Tresse and C. Sternberg, Critical review on biofilm methods, *Crit. Rev. Microbiol.*, 2017, **43**, 313–351.
51 Y. Zhang, A. Xu, X. Lv, Q. Wang, C. Feng and J. Lin, Non-Invasive Measurement, Mathematical Simulation and In Situ Detection of Biofilm Evolution in Porous Media: A Review, *Appl. Sci.*, 2021, **11**, 1391.
52 E. E. Beuling, D. van Dusschoten, P. Lens, J. C. van den Heuvel, H. van As and S. P. P. Ottengraf, Characterization of the diffusive properties of biofilms using pulsed field gradient-nuclear magnetic resonance, *Biotechnol. Bioeng.*, 1998, **60**, 283–291.
53 B. C. Hoskins, L. Fevang, P. D. Majors, M. M. Sharma and G. Georgiou, Selective imaging of biofilms in porous media by NMR relaxation, *J. Magn. Reson.*, 1999, **139**, 67–73.
54 B. Manz, F. Volke, D. Goll and H. Horn, Measuring local flow velocities and biofilm structure in biofilm systems with magnetic resonance imaging (MRI), *Biotechnol. Bioeng.*, 2003, **84**, 424–432.
55 P. D. Majors, J. S. McLean, G. E. Pinchuk, J. K. Fredrickson, Y. A. Gorby, K. R. Minard and R. A. Wind, NMR methods for in situ biofilm metabolism studies, *J. Microbiol. Methods*, 2005, **62**, 337–344.
56 J. S. McLean, O. N. Ona and P. D. Majors, Correlated biofilm imaging, transport and metabolism measurements via combined nuclear magnetic resonance and confocal microscopy, *ISME J.*, 2008, **2**, 121–131.
57 J. S. McLean, P. D. Majors, C. L. Reardon, C. L. Bilskis, S. B. Reed, M. F. Romine and J. K. Fredrickson, Investigations of structure and metabolism within Shewanella oneidensis MR-1 biofilms, *J. Microbiol. Methods*, 2008, **74**, 47–56.
58 R. S. Renslow, P. D. Majors, J. S. McLean, J. K. Fredrickson, B. Ahmed and H. Beyenal, In situ effective diffusion coefficient profiles in live biofilms using pulsed-field

gradient nuclear magnetic resonance, *Biotechnol. Bioeng.*, 2010, **106**, 928–937.
59 B. Zhang and R. Powers, Analysis of bacterial biofilms using NMR-based metabolomics, *Future Med. Chem.*, 2012, **4**, 1273–1306.
60 H. van As and P. Lens, Use of 1 H NMR to study transport processes in porous biosystems, *J. Ind. Microbiol.*, 2001, **26**, 43–52.
61 L. Caizán-Juanarena, J. R. Krug, F. J. Vergeldt, J. M. Kleijn, A. H. Velders, H. van As and A. ter Heijne, 3D biofilm visualization and quantification on granular bioanodes with magnetic resonance imaging, *Water Res.*, 2019, **167**, 115059.
62 S. A. Patil, S. Chigome, C. Hägerhäll, N. Torto and L. Gorton, Electrospun carbon nanofibers from polyacrylonitrile blended with activated or graphitized carbonaceous materials for improving anodic bioelectrocatalysis, *Bioresour. Technol.*, 2013, **132**, 121–126.
63 J. Erben, A. Heußner, S. Thiele and S. Kerzenmacher, Activation of electrospun carbon fibers: the effect of fiber diameter on CO2 and steam reaction kinetics, *J. Polym. Res.*, 2021, **28**, 1–14.
64 J. Erben, X. Wang and S. Kerzenmacher, High Current Production of Shewanella Oneidensis with Electrospun Carbon Nanofiber Anodes is Directly Linked to Biofilm Formation, *ChemElectroChem*, 2021, **8**, 1836–1846.
65 E. Kipf, J. Koch, B. Geiger, J. Erben, K. Richter, J. Gescher, R. Zengerle and S. Kerzenmacher, Systematic screening of carbon-based anode materials for microbial fuel cells with Shewanella oneidensis MR-1, *Bioresour. Technol.*, 2013, **146**, 386–392.
66 M. Loferer-Krössbacher, J. Klima and R. Psenner, Determination of bacterial cell dry mass by transmission electron microscopy and densitometric image analysis, *Appl. Environ. Microbiol.*, 1998, **64**, 688–694.
67 J. Erben, Z. A. Pinder, M. S. Lüdtke and S. Kerzenmacher, Local Acidification Limits the Current Production and Biofilm Formation of Shewanella oneidensis MR-1 With Electrospun Anodes, *Front. Microbiol.*, 2021, **12**, 660474.
68 R. Abboud, R. Popa, V. Souza-Egipsy, C. S. Giometti, S. Tollaksen, J. J. Mosher, R. H. Findlay and K. H. Nealson, Low-temperature growth of Shewanella oneidensis MR-1, *Appl. Environ. Microbiol.*, 2005, **71**, 811–816.
69 J. H. Simpson and H. Y. Carr, Diffusion and Nuclear Spin Relaxation in Water, *Phys. Rev.*, 1958, **111**, 1201–1202.
70 H. Edzes, D. van Dusschoten and H. Van As, Quantitative T2 imaging of plant tissues by means of multi-echo MRI microscopy, *Magn. Reson. Imag.*, 1998, **16**, 185–196.
71 A. Gędas and M. A. Olszewska, in *Recent trends in biofilm science and technology*, ed. M. Simões, A. Borges and L. C. Simões, Academic Press, London, United Kingdom, San Diego, CA, 2020, pp. 1–21.
72 L. Gao, X. Lu, H. Liu, J. Li, W. Li, R. Song, R. Wang, D. Zhang and J. Zhu, Mediation of Extracellular Polymeric Substances in Microbial Reduction of Hematite by Shewanella oneidensis MR-1, *Front. Microbiol.*, 2019, **10**, 575.
73 J. Wei, P. Liang and X. Huang, Recent progress in electrodes for microbial fuel cells, *Bioresour. Technol.*, 2011, **102**, 9335–9344.
74 K. Dolch, J. Danzer, T. Kabbeck, B. Bierer, J. Erben, A. H. Förster, J. Maisch, P. Nick, S. Kerzenmacher and J. Gescher, Characterization of microbial current production as a function of microbe-electrode-interaction, *Bioresour. Technol.*, 2014, **157**, 284–292.
75 K. Muffler and R. Ulber, *Productive Biofilms*, Springer International Publishing, Cham, 2014.
76 J. Yang, S. Cheng, P. Li, H. Huang and K. Cen, Sensitivity to Oxygen in Microbial Electrochemical Systems Biofilms, *iScience*, 2019, **13**, 163–172.
77 M. Lu, S. Chan, S. Babanova and O. Bretschger, Effect of oxygen on the per-cell extracellular electron transfer rate of Shewanella oneidensis MR-1 explored in bioelectrochemical systems, *Biotechnol. Bioeng.*, 2017, **114**, 96–105.
78 W. Bogner, R. Otazo and A. Henning, Accelerated MR spectroscopic imaging—a review of current and emerging techniques, *NMR Biomed.*, 2021, **34**, 0952–3480.
79 P. van Zijl and N. Yadav, Chemical exchange saturation transfer (CEST): what is in a name and what isn't?, *Magn. Reson. Med.*, 2011, **65**, 927–948.
80 M. Holz, Electrophoretic NMR, *Chem. Soc. Rev.*, 1994, **23**, 165–174.
81 P. Stilbs and I. Furó, Electrophoretic NMR, *Curr. Opin. Colloid Interface Sci.*, 2006, **11**, 3–6.